PHYSICAL REVIEW B **83**, 075304 (2011)

Ballistic transport and boundary scattering in InSb/$In_{1-x}Al_xSb$ mesoscopic devices

A. M. Gilbertson,[1,*] M. Fearn,[2] A. Kormányos,[3] D. E. Read,[1] C. J. Lambert,[3] M. T. Emeny,[2] T. Ashley,[2] S. A. Solin,[1,4] and L. F. Cohen[1]

[1]*Blackett Laboratory, Imperial College London, Prince Consort Road, London, SW7 2BZ, United Kingdom*
[2]*QinetiQ, St. Andrews Road, Malvern, Worcestershire, WR14 3PS, United Kingdom*
[3]*Department of Physics, Lancaster University, Lancaster, LA1 4YB, United Kingdon*
[4]*Center for Material Innovations and Department of Physics, Washington University in St. Louis, Saint Louis, Missouri 63130, USA*

(Received 14 September 2010; revised manuscript received 23 November 2010; published 8 February 2011)

We describe the influence of hard-wall confinement and lateral dimension on the low-temperature transport properties of long diffusive channels and ballistic crosses fabricated in an InSb/$In_{1-x}Al_xSb$ heterostructure. Partially diffuse boundary scattering is found to play a crucial role in the electron dynamics of ballistic crosses and substantially enhance the negative bend resistance. Experimental observations are supported by simulations using a classical billiard ball model for which good agreement is found when diffuse boundary scattering is included.

DOI: 10.1103/PhysRevB.83.075304 PACS number(s): 73.23.Ad, 73.63.Hs

I. INTRODUCTION

The InSb two-dimensional electron gas (2DEG) is attractive for room-temperature (RT) applications such as high-speed logic devices[1] and high spatial resolution magnetic-field sensors,[2] where carrier mobility plays an important role. Recent improvements in the growth of InSb/$In_{1-x}Al_xSb$ quantum wells (QWs) on GaAs substrates have lead to RT electron mobility values in excess of $\mu = 6\ m^2/V\,s$ approaching the phonon-limited value of $7\ m^2/V\,s$.[3] For applications requiring high spatial resolution, device miniaturization inevitably leads to the relevant lateral dimensions of the conducting channel becoming comparable to the mean free path (λ_0), where transport is ballistic. In this regime the bulk properties of the 2DEG are no longer preserved. Therefore, it is essential to understand how the InSb 2DEG properties are altered when fabricated at the nanoscale. For example, in long InAs/AlSb 2DEG channels fabricated using reactive-ion etching (RIE), the mobility is degraded from that in the bulk owing to top surface damage caused by energetic ions, but the RIE-induced sidewall roughness degrades the mobility further as the width of the channel (w) is reduced below λ_0 owing to electron-boundary scattering.[4] Degradation of μ is detrimental to the performance of transistors, conventional Hall, and extraordinary magnetoresistor sensors based on diffusive transport, but it is not clear how properties are further effected in the mesoscopic regime. Lateral depletion of conducting channels, or sidewall depletion, is also relevant as devices are miniaturized. With the exception of the InAs system that exhibits very little sidewall depletion,[5] Fermi-level pinning at the surface of mesa-etched III-V devices can lead to substantial sidewall depletion, which is often not straightforward to deduce. Knowledge of the depletion width (w_{dep}) is essential in order to determine the true *effective* electrical width (w_{eff}) of narrow channel devices, e.g., submicrometer Hall sensors[6] and quasi-1D wires.[7] Here we present a comprehensive study on the effect that fabricating high-mobility InSb/InAlSb structures with critical dimensions less than the mean free path has on the transport properties.

When the length of the channel (l) is reduced below the mean free path ($l < \lambda_0$), electrons can traverse the device without scattering internally. Ballistic transport in GaAs/$Al_xGa_{1-x}As$ microjunctions (where $l, w < \lambda_0$) has been widely studied at low temperatures and by using the Landauer-Büttiker (LB) formalism[8] a good understanding of the phenomena is established.[9,10] In particular, a variety of distinct departures from classical behavior appear in the low-field magnetotransport of simple cross junctions, such as a negative resistance in zero magnetic field referred to as "bend resistance,"[11,12] and a quenched or negative Hall resistance at low fields.[13] The above-mentioned anomalies, at least when the number of transverse modes, N, is much larger than one ($N \gg 1$), can be adequately described by combining the LB formalism and a classical approach, whereby electrons are treated as classical particles which, by analogy to ray optics, reflect from the boundaries with predictable trajectories.[14]

The mesoscopic properties of InSb and its heterostructures are still relatively unexplored.[15] Negative bend resistance (NBR) was reported in InSb/$In_{1-x}Al_xSb$ submicrometer structures up to $T \leqslant 205$ K.[16] Above this temperature (where NBR was expected to persist), it was proposed that parallel conduction in the heterostructure masks the ballistic component from the 2DEG. Indeed, a recent study of transport in similar InSb/$In_{1-x}Al_xSb$ samples showed that at elevated temperatures, intrinsic conduction in the ternary buffer layer contributes up to ≈5% of the total conduction.[17] The significance of such parallel conduction is accentuated in shallow etched submicrometer structures, where the volume of the remaining buffer layer is large. This technological problem may be overcome by an improved heterostructure design. Therefore, two regimes are identified in InSb/$In_{1-x}Al_xSb$ submicrometer structures: (a) low temperatures (<100 K), where ballistic transport in the 2DEG is dominant and (b) high temperatures (>150 K) where as yet, in all reported structures, parasitic intrinsic conduction in the buffer layer occurs.

We emphasize that the interaction of charge carriers with the device boundaries plays a central role in determining the characteristics of submicrometer devices, and a proper investigation in the InSb 2DEG system has not been made; in particular, ballistic anomalies are acutely sensitive to the device dimension, geometry,[18] and the specularity of the boundary scattering.[19,20] Accordingly, we report here

a detailed study of the influence of device size, sidewall depletion, and boundary scattering on the magnetotransport properties of InSb/$In_{1-x}Al_xSb$ mesoscopic structures with hard-wall confinement. For the purpose of this article, we present data from long channels ($l > \lambda_0$) and submicrometer crosses with lateral dimensions down to $w \approx 170$ nm, and we restrict ourselves to low temperatures where intrinsic conduction is negligible. A detailed analysis of the ballistic transport anomalies and the agreement with theory is presented with the aid of a classical billiard ball model.

II. EXPERIMENTAL METHODS

Devices were fabricated from a single-modulation-doped InSb/$In_{1-x}Al_xSb$ QW heterostructure grown by molecular-beam epitaxy onto a GaAs (001) substrate. In the growth sequence, the sample consists of an AlSb (200 nm)/$In_{0.9}Al_{0.1}Sb$ (3 μm) buffer layer, a 30-nm InSb QW, and a 50-nm $In_{0.85}Al_{0.15}Sb$ cap in which a single Te δ-doping layer is located, 20 nm above the top of the QW. Figure 1(d) shows the self-consistent Schrödinger-Poisson solution for the conduction-band profile and the energy levels in the QW. The properties of the as-grown 2DEG were determined from a 40-μm-wide Hall bridge (control sample) fabricated using conventional wet etching. At 2 K the 2D electron density (n) and mobility (μ) were $n = 3.95 \times 10^{15}$ m^{-2} and $\mu = 19.5$ m^2/V s, corresponding to a mean free path of $\lambda_0 = \hbar k_F \mu / e = 2.03$ μm and a Fermi wavelength of 40 nm [$k_F = (2\pi n)^{1/2}$ is the Fermi wave vector]. The bulk magnetotransport properties of this and similar samples were recently reported.[3,17] At low temperatures relevant to this study, the mobility was found to be limited by remote ionized impurity scattering from the Te δ-layer. Measurements were performed with the sample in the dark using a low-frequency lock-in technique (currents between 100 and 500 nA) and with B applied perpendicular to the plane of the 2DEG.

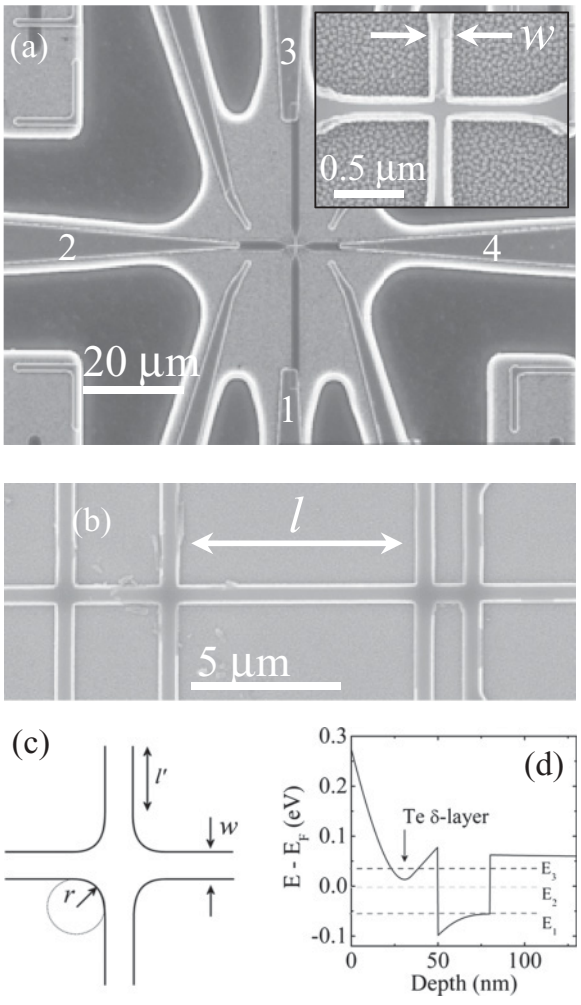

FIG. 1. Electron micrographs of (a) a typical device structure showing the leads and contact arrangement for a cross, and (b) a 550-nm-wide Hall bridge. Inset to (a): A $w = 171$ nm cross. (c) A schematic of the Hall cross geometry. (d) A self-consistent Schrödinger-Poisson solution for the conduction-band profile of the heterostructure showing the confined energy levels.

Hall crosses and Hall bridges with varying w were patterned by electron-beam lithography using a negative tone resist as an etch mask. Pattern transfer was achieved using an inductively coupled plasma RIE in a CH_4/H_2 gas mixture at a pressure of 10 mTorr, forming shallow mesas of $\approx$135 nm depth that provide hard-wall confinement. The process parameters yielded an etch rate of the ternary $In_{0.85}Al_{0.15}Sb$ compound of $\approx$10 nm/min. Ti/Au ohmic contacts were made using standard optical lithography and a cold shallow contacting technique.[21] A deep wet chemical etch was used to remove the entire 3-μm-thick buffer layer surrounding the device and contacts; the volume of the remaining buffer layer beyond the shallow boundaries of the structures was minimized by mask design and controlled lateral etching [see Fig. 1(a)]. Electron micrographs of a $w = 171 \pm 10$ nm cross and $w = 550 \pm 10$ nm Hall bridge are shown in Figs. 1(a) and 1(b) [the uncertainty in w is owing to a residual polymer deposit from the RIE at the mesa edge (fencing)]. The junction corners are nominally square, but a small unavoidable rounding of the corners (<50 nm radius) results from the large proximity effect in the e-beam lithography of InSb.

III. CLASSICAL BILLIARD BALL MODEL

To interpret our results presented in the following section, we simulate the bend and Hall resistance of the cross junction following the classical model of Beenakker and van Houten that treats electrons as classical particles (billiard balls) reflecting from the device boundaries.[14] The resistance in the ballistic regime is expressed in terms of the transmission probabilities between the various leads by the LB formula.[8] We consider the four-terminal cross geometry with fourfold symmetry, in which case, respectively, the Hall and bend resistances, R_H and R_B are given by d1

$$R_H = R_0 \frac{T_R^2 - T_L^2}{(T_R + T_L)[(T_R + T_F)^2 + (T_L + T_F)^2]} \quad \text{(1a)}$$

and d2

$$R_B = R_0 \frac{T_L T_R - T_F^2}{(T_R + T_L)[(T_R + T_F)^2 + (T_L + T_F)^2]}, \quad \text{(1b)}$$

where T_F, T_L, and T_R are the probabilities of an electron transmitted from the injection lead (arbitrary) to the

forward, left-hand, and right-hand leads, respectively, and $R_0 = h/2e^2N$ with N equal to the number of transverse modes at the Fermi energy. The geometry of the cross junction is shown in Fig. 1(c) and is defined by three parameters: the lead width w, lead length l', and radius of curvature of the corners, r, with $r^2 = x^2 + y^2$ in the plane. For the purposes of our calculations, we use a hard-wall confining potential (infinite potential barriers at the boundaries). This is a good approximation for wider leads, greater than 200 nm in width, in which the potential is very flat in the center of the channel and increases rapidly near the boundaries.[22] In the semiclassical limit and for hard-wall confinement, N is given by $N = k_F w/\pi$. All calculations presented are for $N \gg 1$, where the model is strictly valid.

The transmission and reflection coefficients are calculated by injecting a large number of classical particles (5×10^4) from a specified injection lead uniformly across the lead with an angular distribution $P(\phi) = \frac{1}{2}\cos(\phi)$ (ϕ being the angle with respect to the lead axis).[14] The trajectories of the particles are determined via integration of the equations of motion using the Verlet technique until they exit the junction via one of the four leads. Particles are injected into the junction region at the Fermi velocity $v_F = \hbar k_F/m^*(E)$ with an effective mass $m^*(E)$, which takes into account modifications owing to band nonparabolicity within an analytical model for the dispersion, $E(1 + \alpha E) = \hbar^2k^2/2m^*$, where α is the nonparabolicity parameter.[23] For the InSb QW studied here, we use a subband-edge effective mass $m^*_{sb} = 0.0162$ and a nonparabolicity parameter of α=3.8 eV^{-1}, which gives a fit to an eight-band $k \cdot p$ model of a 30-nm QW with $In_{0.85}Al_{0.15}Sb$ barriers to within a few meV over a 100-meV range.

We incorporate diffuse boundary scattering into the model using the approach of Blaikie *et al.*[20] Boundary scattering is captured using a single specularity parameter, p, that describes the probability of a particle scattering diffusively $(1 - p)$ from a boundary. After a diffuse scattering event, particles are reinjected at the collision point with an angle $-\pi/2 \leqslant \theta \leqslant \pi/2$ from the boundary normal chosen randomly from a uniform distribution. Within this model, the transmission coefficients are sensitive to the lead length l' as this directly affects the number of interactions with the boundary.

IV. RESULTS AND DISCUSSION

A. Diffuse properties in long channels

Fluctuations in the electrostatic potential profile of a conducting channel can alter the transport properties via electron-boundary scattering, particularly in submicrometer devices where the channel width $w \leqslant \lambda_0$ and electrons can travel ballistically between the channel boundaries.

Electron-boundary scattering can be characterized by two parameters: the specularity parameter p and λ_B, the average distance an electron travels before the probability of it scattering diffusively is equal to one.[19] In general, $p < 1$ for both mesa-etched and split-gate devices.[19,24] λ_B is proportional to w, so that, as w is reduced, the electron-boundary interactions manifest in the transport properties. An increased backscattering in narrow channels enhances the zero-field longitudinal resistance $R_{xx}(0)$, resulting in an effective μ that is reduced from that measured in a wide sample. Further, for partially diffuse scattering ($p < 1$), a distinctive low field peak appears in $R_{xx}(B)$ (discussed in Sec. IV C).[10]

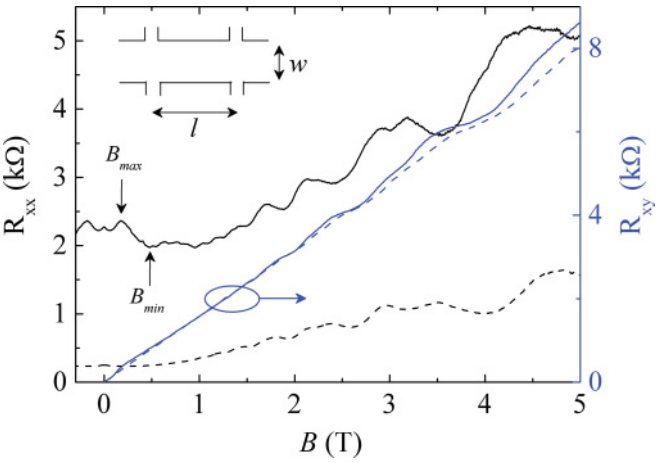

FIG. 2. (Color online) Longitudinal R_{xx} (left-hand axis) and transverse R_{xy} (right-hand axis) magnetoresistance of $w = 550$ nm (solid lines) and 3 μm (dashed lines) Hall bridges at 2 K ($l = 8.4$ μm). Inset: A schematic of the device structure and the relevant dimensions. The positions of B_{max} and B_{min} relate to features associated with boundary scattering (see the text).

Measurements were performed on long channels in the Hall bridge geometry [Fig. 1(b) and inset to Fig. 2] with a longitudinal voltage lead separation of $l = 8.4$ μm ($>\lambda_0$) ensuring that transport is diffusive along the channel. In Fig. 2 we show the longitudinal R_{xx} and transverse R_{xy} resistance as a function of magnetic field at 2 K for a 3-μm and 550-nm-wide Hall bridge. Shubnikov de-Haas (SdH) oscillations in R_{xx} are observed in each device superposed onto an increasing background resistance related to parallel conduction in the upper barrier.[17] The 2D electron density n is determined from the periodicity of SdH oscillations and the mobility μ from the zero field resistance, according to $\mu = l/wR_{xx}(0)ne$. The experimental n, μ, and the corresponding mean free paths for the 3-μm and 550-nm-wide Hall bridges are given in Table I, together with the properties of the control sample ($w =$ 40 μm). A monotonic decrease in n and μ is observed as w is reduced. The reduction in n is attributed to the lateral potential formed by a sidewall depletion region (discussed further in Sec. IV B), in addition to the lateral confinement imposed on narrow channels that raise the conduction-band edge in the center of the channel as w is reduced, hence depleting the 2DEG. The observed degradation of μ is consistent with the presence of boundary scattering, which becomes increasingly

TABLE I. Properties of the InSb 2DEG obtained from Hall bridges with varying physical width w at 2 K. Data for $w = 40$ μm represents the control sample.

w (μm)	40	3	0.55
$n(10^{15}m^{-2})$	3.95	3.9	3.77
μ (m^2/V s)	19.5	17.95	14.8[a]
λ_0 (μm)	2.03	1.85	1.50[a]

[a]Calculated using the effective electrical width determined in Sec. IV B.

important as w is reduced. Nevertheless, the mobility in the 550-nm-wide channel is only degraded by ≈25% with respect to the control sample, with a corresponding mean free path of $\lambda_0 = 1.5\ \mu$m. Ballistic transport is therefore expected in the submicrometer crosses ($\lambda_0 > w$), discussed in Sec. IV D.

B. Determination of depletion width

An important parameter of narrow channels is the electrical width w_{eff}. Owing to the Fermi energy pinning in the band gap at the air interface, sidewall depletion is frequently observed for narrow mesa-etched channels resulting in a w_{eff} that can be substantially smaller than the physical width, w.[7,25] The difference is equal to the sum of the lateral depletion width at each boundary (w_{dep}). Knowledge of w_{dep} is essential for many applications but is not straightforward to gain. We found that devices with $w \leqslant 134$ nm were electrically depleted over the entire temperature range. This puts an initial estimate on the depletion width at $w_{\text{dep}} \approx 67$ nm. We can also determine w_{eff} from tracking the depopulation of quasi-1D magnetoelectric subbands in the low-field R_{xx} data of narrow channels.[26] Similar to 2D Landau levels, these hybrid subbands depopulate with increasing field, but do so at a slower rate, as evidenced by a nonlinear subband index (i) versus $1/B$ plot in the low-field region. For a parabolic confining potential, the magnetic depopulation of subbands can be described analytically by[26]

$$i \approx \left[\frac{3\pi}{4} N_{1\text{D}}\omega_0 \left(\frac{\hbar}{2m*}\right)^{1/2}\right]^{2/3} \frac{1}{\omega}, \tag{2}$$

where N_{1D} is the 1D electron density, ω_0 is the characteristic frequency defining the strength of the confinement, and $\omega = (\omega_c^2 + \omega_0^2)^{1/2}$, where $\omega_c = eB/m^*$ is the cyclotron frequency. One can see that for small fields, the dependence of i on $1/B$ is nonlinear and for large fields, $\omega \rightarrow \omega_c$, and i is proportional to $1/B$ as in the usual 2D case. As noted in Ref. 26, a square-well potential is more appropriate for wider channels, nevertheless, the model expressed in Eq. (1b) provides valuable insight into the effective width of the channel. A subband depopulation diagram for the 550-nm-wide Hall bridge is shown in Fig. 3. A pronounced departure from linear in $1/B$ behavior (dashed line) is observed below 1 T. The solid line in Fig. 3 represents a least-squares fit of Eq. (1b) to the data using an effective mass at the Fermi energy of $m^* = 0.022m_0$ (we found that the fitting results are relatively insensitive to small changes of ±10% in m^*). From this fit we deduce a confinement energy $\hbar\omega_0$ and N_{1D} of 2.6 meV and 3×10^9 m^{-1}, respectively. The effective width is then estimated from[26]

$$w_{\text{eff}} = 2\pi N_{1\text{D}}^{1/3} \left(\frac{2\hbar}{3\pi m^*\omega_0}\right)^{2/3}. \tag{3}$$

Substituting the values of ω_0 and N_{1D} into (2), we determine $w_{\text{eff}} = 414 \pm 5$ nm. This implies a depletion width of $w_{\text{dep}} = (w - w_{\text{eff}})/2 = 68 \pm 6$ nm, which is in remarkably good agreement with the estimate made directly from the observed electrical depletion of devices of $w < 134$ nm.

Finally, we remark on a separate and consistent estimate of w_{eff} made from a classical size effect (with no assumption of confining potential). Electron backscattering in narrow channels that enhances $R_{xx}(0)$ is suppressed by a perpendicular magnetic field owing to the formation of localized edge states or classical skipping orbits at the boundaries. This leads to a negative MR peaked at $B = 0$, persisting until $B_{\text{min}} = 2B_0$, where $B_0 = \hbar k_F/ew_{\text{eff}}$ is the field when the cyclotron radius, $R_c = \hbar k_F/eB$, equals w_{eff}. At this point a marked change in slope is expected.[27] As seen in Fig. 2 (and more clearly in Fig. 4), this behavior is observed in our data. A kink in the low-field MR is observed at a field $B_{\text{min}} \approx 0.5$ T (indicated by an arrow), from which we estimate $w_{\text{eff}} \approx 406$ nm (i.e., $w_{\text{dep}} \approx 72$ nm). This estimate is consistent with the value obtained

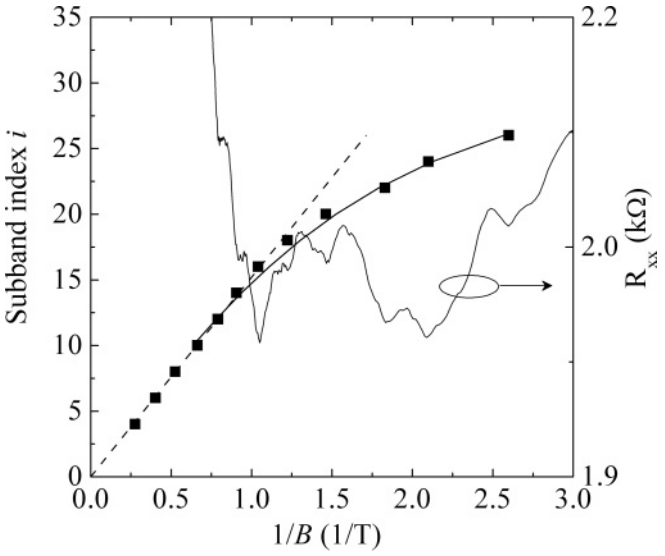

FIG. 3. Subband depopulation diagram for the $w = 550$ nm Hall bridge at 2 K. The faint solid line shows the corresponding R_{xx} data (right-hand axis) from which the subband indices (left-hand axis) were assigned. The dashed and solid lines represent fits of Eq. (1b) to the high-field linear portion of the data and the low-field nonlinear portion of the data, respectively.

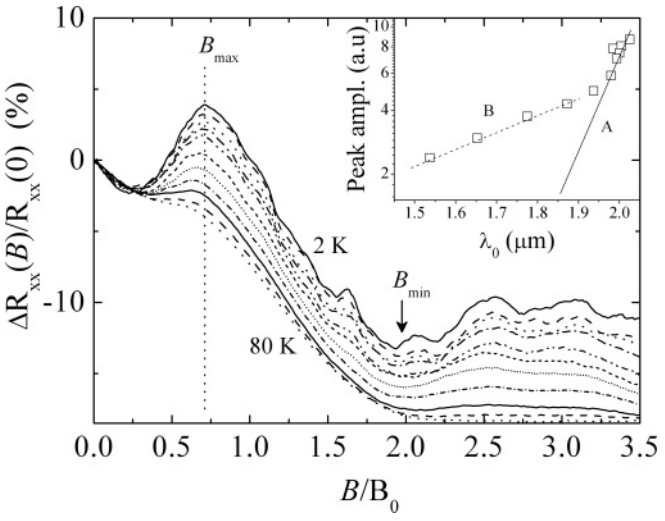

FIG. 4. Magnetoresistance, $\Delta R_{xx}(B)/R_{xx}(0)$, of the $w = 550$ nm Hall bridge plotted against the normalized field B/B_0 at various temperatures after subtraction of a linear background displaying a peak at B_{max}. Inset: The peak amplitude plotted against the mean free path (λ_0) in the control sample at each temperature.

from the magnetodepopulation analysis, adding confidence to our estimate of w_{dep}.

C. Partially diffuse boundary scattering in narrow channels

The specularity of the boundary scattering plays a crucial role in the transport of submicrometer devices. In particular, Blaikie *et al.*[20] showed that resistance anomalies in ballistic devices can be enhanced substantially by partially diffuse boundary scattering. The specularity of boundary scattering can be studied from measurements on long narrow channels ($w \leqslant \lambda_0$), where electron-boundary interactions manifest in the resistance. It has been shown that partially diffuse boundary scattering leads to an anomalous peak in R_{xx} at small fields ($0 < B < B_{min}$) with a position (B_{max}) that scales inversely with w.[19,28,29] As seen in Fig. 2, a pronounced peak is distinguished in the low-field R_{xx} of the $w = 550$ nm Hall bridge at $B_{max} \approx 180$ mT (indicated by the arrow). We note that a low-field peak with an entirely different origin was also predicted[14] and experimentally observed[30] in the MR of ballistic Hall bridges where $l < \lambda_0$. In our case, $l \gg \lambda_0$, so that the measurement is in the diffusive regime and the observed peak can be unambiguously attributed to partially diffuse boundary scattering.

In Fig. 4 we show the low-field MR of the $w = 550$ nm Hall bridge $[R_{xx}(B) - R_{xx}(0)]/R_{xx}(0)$ plotted against the normalized field B/B_0 (using $w_{eff} = 414$ nm) at various temperatures between 2 and 80 K after subtraction of the high-field quasilinear background. The classical model for in-plane MR of thin metal films (where the film thickness $t \leqslant \lambda_0$ and $p = 0$) predicts that $B_{max} = 0.55B_0$, i.e., when $R_c = w_{eff}/0.55$. This has since been considered as a method of estimating w_{eff}.[28–30] We have found that the boundary scattering peak occurs at a somewhat larger value, $B_{max} \approx 0.7B_0$. It follows that estimating w_{eff} from the classical prediction,[28] $w_{eff} = 0.55R_c$, yields a value significantly less than that obtained in the previous section. Given that the calculations of B_{max} are sensitive to the details of the model[30] and that predicted values have been reported in the range $0.55B_0 \leqslant B_{max} \leqslant B_0$,[30,31] we suggest that this method provides a less reliable estimate of w_{eff}.

The decay of the peak at B_{max} with temperature is associated with the reduction of λ_0 in the bulk of the channel (taken from the control device where boundary scattering can be neglected) below λ_B.[19] The boundary scattering length is estimated (rather arbitrarily) by assuming that $\lambda_B \approx \lambda_0$ (in the bulk of the channel) at the temperature (T') when $\Delta R_{xx}(B_{max})/R_{xx}(0) = 1$.[24] Taking $T' \approx 40$ K corresponds to $\lambda_B \approx 1.75$ μm. The specularity parameter p is then estimated from the empirical relationship $1 - p \approx w_{eff}/\lambda_B$, yielding $p \approx 0.71$ for the $w = 550$ nm ($w_{eff} = 414$ nm) Hall bridge. The inset of Fig. 4 shows the amplitude of the peak at B_{max} plotted against λ_0 (obtained from the control sample at each temperature). The amplitude was extracted with respect to a straight line drawn between data at $B/B_0 = 0$ and $B/B_0 = 2$. λ_B may then be interpreted as the value of λ_0 when the peak amplitude decays to zero. Two dependences on λ_0 are distinguished in the data: a rapid decay (solid line) labeled as A and a slower decay (dashed line) labeled as B. We broadly separate these into the regimes where remote ionized impurities and phonons dominate momentum scattering in the bulk of the channel, respectively. We consider regime B unsuitable for this analysis because large-angle phonon scattering randomizes the electrons' momentum, in addition to diffuse boundary scattering events that alter λ_B. Therefore, only at low temperatures (regime A) can information on λ_B be extracted with confidence. In regime A, we extrapolate a value of $\lambda_B \approx 1.85$ μm, giving $p \approx 0.77$, which is similar to the previous estimate. We conclude from our analysis that $p \approx 0.7$–0.8.

The value of p is expected to be a property of the boundaries themselves and therefore be the same for devices fabricated in the same way. Given the assumptions made in order to estimate p, emphasis should not be on the value of p itself, but rather it should be sufficient that one observes the characteristic low-field MR features shown in Figs. 2 and 4, to conclude that partially diffuse boundary scattering is significant and $p < 1$.

D. Ballistic transport in cross junctions

We now turn to the experimental results in ballistic crosses formed from two intersecting channels of width w [see inset to Fig. 1(a)], where the relevant lateral dimensions ($L \approx w$) are substantially less than the mean free path. We present the results from four crosses with physical widths [inferred from inspection of scanning electron micrographs] of $w = 924$, 550, 400, and 171 ± 10 nm. The inferred effective electrical widths $w_{eff} = w - 2w_{dep}$ are given in Table II, where we have used the depletion width determined in Sec. IV B ($w_{dep} = 68$ nm). Note that the smallest cross ($w = 171$ nm) has an estimated electrical width of $w_{eff} \approx 35$ nm, which is among the narrowest conducting mesa-etched devices reported.[5]

Figure 5 shows the results for the Hall resistance $R_H = V_{4,2}/I_{1,3}$ [the lead arrangement is shown in Fig. 1(a)] as a function of B for the crosses. Here V_{ij} and I_{mn} indicate the voltage of terminal i measured with respect to j when current is passed from terminal m to n, respectively. Data for $w = 924$, 550, and 400 nm were taken at 2 K and the $w = 171$ nm at 40 K (the $w = 171$ nm junction became depleted for $T < 30$ K). Quantum Hall plateaus are resolved in the data from the largest three crosses. The electron densities are determined from fits of the classical 2D result $R_H(B) = -B/ne$ (indicated by the dashed lines in Fig. 5) to the high-field linear portions of data. $R_H(B)$ for the $w = 171$ nm cross is strikingly different—no obvious quantization of R_H occurs over the entire field range (thermal broadening) and $R_H(B)$ is nonlinear up to $|B| \approx 4$ T, making the determination of n less trivial. The extracted electron densities of the crosses are listed in Table II. The dependence of n on w_{eff} is presented in the bottom inset to Fig. 5, including data from wider Hall bridges.

At low fields, $|B| < 1$ T, clear anomalies appear in R_H for all crosses (top inset to Fig. 5)—the development of the anomalies with decreasing w is clear. No suppression of R_H at approximately $B = 0$ is observed in the largest three crosses (only a very small reduction is found for the $w = 400$ nm cross). In the smallest cross (blue line) the effect is striking; R_H is completely quenched *and negative* (positive in our configuration) up to $|B| < 0.65$ T. A small asymmetry in $R_H(B)$ is observed in all cases, which is attributed to geometric asymmetries in the junction. The appearance of quenching

TABLE II. Relevant parameters for the ballistic crosses and parameters used in the billiard calculations. Effective widths $w_{\rm eff} = w - 2w_{\rm dep}$ were calculated using $w_{\rm dep} = 68$ nm determined in Sec. IV B.

w (nm)	$w_{\rm eff}$ (nm)	n (10^{15} m^{-2})	N	R_0 (Ω)	B_0 (T)	r (nm)	l' (μm)	p
924	788	3.85	39	332	0.13	100	2.5	0.79
550	414	3.77	20.3	638	0.25	100	1.5	0.8
400	264	3.1	11.7	1104	0.35	100	1.2	0.69
171	35	2.25	1.3	9775	2.24	—	0.8	—

is of interest with respect to the geometry of the junction. Baranger and Stone[32] showed that generic quenching of R_H occurs only in junctions with rounded corners. This is a consequence of the horn collimation effect[33] that results in a nonequilibrium momentum distribution that enhances the forward transmission (T_F) at the expense of the transmission into the left (T_L) and right (T_R) leads [cf. Eq. (1a)]. Electron collimation was experimentally verified by Molenkamp *et al.*[34] and is a key concept in describing ballistic anomalies, as we demonstrate here. Likewise, the negative R_H results from rebound trajectories (directing electrons into the "wrong" lead for a given field direction) that are only effective in rounded junctions when the radius of curvature of the junction corner (r) is large compared to the lead width, i.e., $r/w > 1$.[18,35] The appearance of these features in the $w = 171$ nm cross is therefore a clear signature of both significant rounding and collimation. Conversely, the lack of quenching in the largest three crosses implies that $r/w_{\rm eff}$ is small, i.e., the junctions are approximately square, as intended. In this respect, the apparent rounding in the 171-nm cross is perhaps surprising; however, if we assume that r must be at least $w_{\rm dep}$, then the lower bound for r is $\approx$70 nm. In this case, $r/w_{\rm eff} > 1$ for the smallest cross and <1 for the larger crosses, accounting for our observations. Some small additional rounding is inevitable in the e-beam and etch process [$<$50 nm radius from the inset to Fig. 1(a)], putting our experimental estimate of r at 120 nm $> r >$ 70 nm.

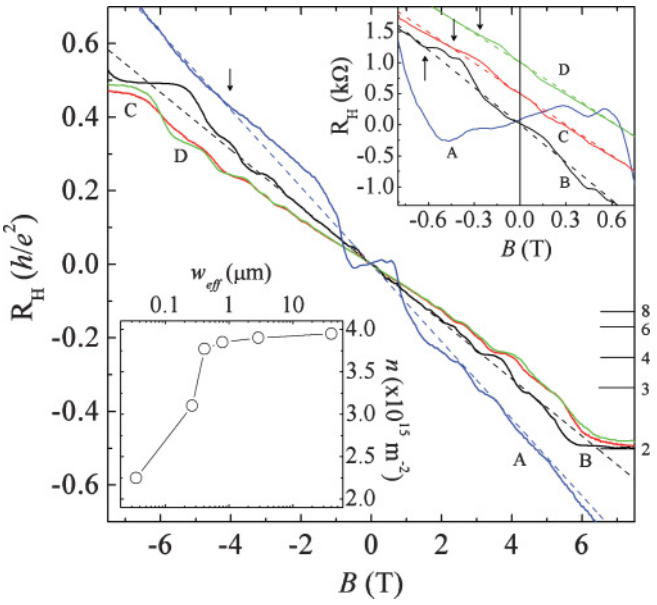

FIG. 5. (Color online) The Hall resistance R_H in units of h/e^2 as a function of B for a $w = 171$ nm (blue line, A), 400 nm (black line, B), 550 nm (red line, C), and 924 nm (green line, D) cross. The dashed lines represent the classical 2D result. Top inset: Low-field data illustrating the anomalies in R_H. Data for the $w = 550$ and 924 nm crosses are offset by 0.5 kΩ for clarity. Bottom inset: Dependence of n on the inferred effective width $w_{\rm eff} = w - 2w_{\rm dep}$ of the devices (crosses and bridges).

Beyond the quenched region, R_H rises above its classical value (dashed lines in Fig. 5) in all devices, marking the onset of the classical "last plateau."[13,18] At larger fields still, $R_H(B)$ rejoins the classical Hall resistance (indicated by the arrows in Fig. 5). For the $w = 171$ nm cross the nonlinearity persists up to $|B| \approx 4$ T. The sharp rise in $R_H(B)$ above its classical value results from trajectories that *guide* electrons into a side lead with minimal boundary reflections, thereby enhancing the asymmetry between T_L and T_R.[14] When guiding is fully effective, electrons are no longer reflected back into the junction (skipping orbits along the junction perimeter) and $T_F, T_R \ll T_L \approx 1$ for $B > 0$. With reference to Eq. (1a), in this regime $R_H(B)$ is predicted to plateau at a value equal to the contact resistance of the lead $R_0 = h/2e^2N$. Classical behavior is then recovered for $B \geqslant 2B_0$. Although a clear plateau region is not observed in our experimental data, features consistent with the predictions of the classical model are observed. For example, the estimated value $2B_0 = 4.5$ T for the $w = 171$ nm cross coincides approximately with the field at which the experimental data rejoin the classical Hall slope. Similar agreement is found for each cross, indicating that our estimates of $w_{\rm eff}$ and k_F are close to their true values (R_0 and B_0 for each cross are listed in Table II).

In Fig. 6(a) we show low-field results obtained in the bend resistance configuration $R_B = V_{4,3}/I_{1,2}$ for the crosses (again, data for the $w = 171$ nm cross was obtained at 40 K). A substantial NBR peak centered at approximately $B = 0$ is observed in all devices, which increases as w is reduced. Asymmetries in the field dependence are also observed in this configuration and are particularly evident in the data for $w =$ 400 nm cross [solid black line in Fig. 6(a)]. To ascertain the origin of the asymmetries, measurements were repeated with the current and voltage leads interchanged. Representative data for the $w = 400$ nm cross is shown by the dashed black line in Fig. 6(a). One can see that the reciprocity relation $R_{mn,ij}(B) = R_{ij,mn}(-B)$ is obeyed, demonstrating that the field asymmetries indeed originate from asymmetries in the junction geometry.[8] This is representative of each device measured.

The origin of NBR is well established: It arises from "straight through" trajectories that raise the potential at lead 3 with respect to lead 4 [see Fig. 1(a)], resulting in a negative resistance. This corresponds to $T_F \gg T_L, T_R$ in the LB formula [cf. Eq. (1b)]. In a small magnetic field, the Lorentz force curves the trajectories into the "correct" lead 4 and the NBR decays to zero, producing a characteristic negative peak (for

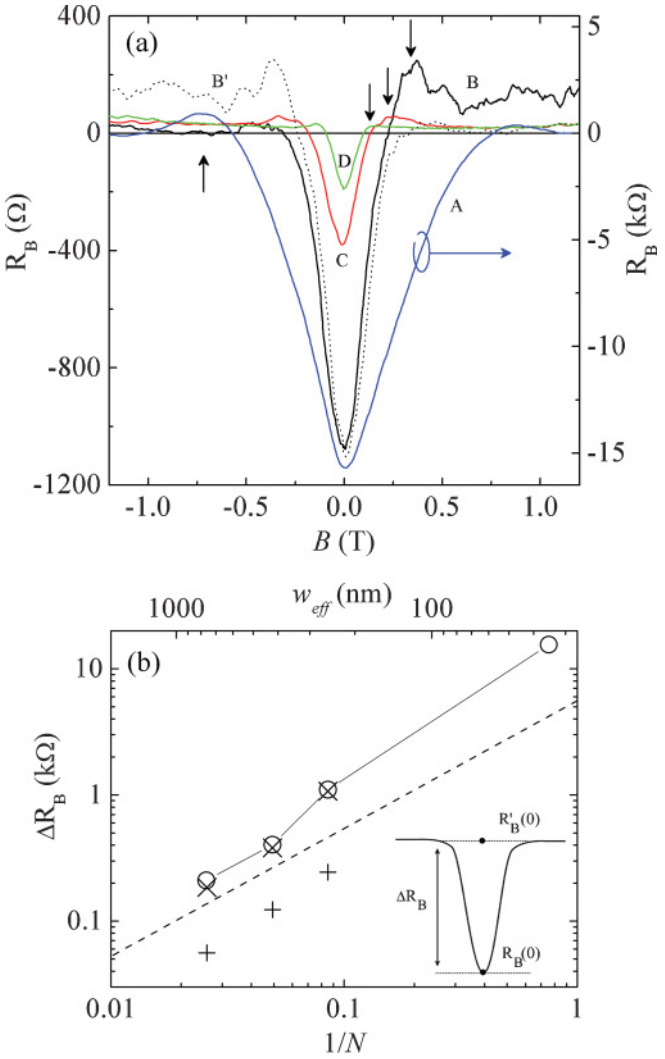

FIG. 6. (Color online) (a) Bend resistance $R_B = V_{4,3}/I_{1,2}$ as a function of magnetic field for a $w = 171$ nm (blue line, A), 400 nm (black line, B), 550 nm (red line, C), and 924 nm (green line, D) cross. The $w = 171$ nm data is plotted on a different scale for ease of comparison. The dotted curve (B′) is the reciprocal measurement $R_{B'} = V_{1,2}/I_{4,3}$ for the $w = 400$ nm cross, illustrating that asymmetries in B originate from junction asymmetry. (b) Dependence of the experimental NBR amplitude ΔR_B (◯) on $1/N = \pi/k_F w_{\text{eff}}$ and w_{eff}. The results from billiard model simulations using the parameters given in Table II (x) and results for $p = 1$ (+) are also shown. The dashed line is a guide to the eye, illustrating a $1/N$ dependence. Inset: A schematic showing the definition of ΔR_B.

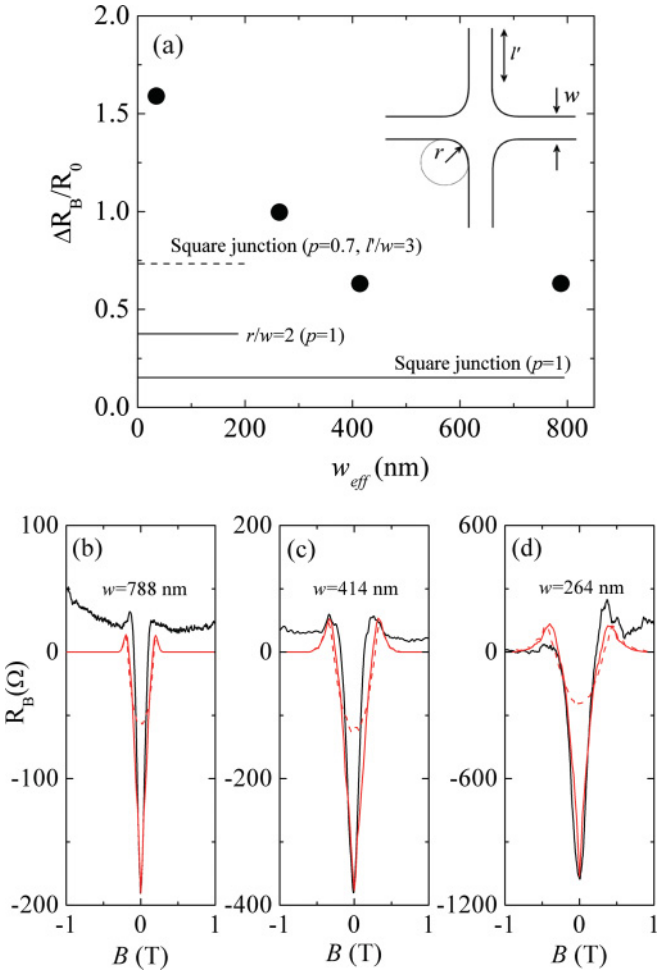

FIG. 7. (Color online) (a) Normalized NBR amplitude $\Delta R_B/R_0$ of the crosses plotted against w_{eff}. Horizontal lines represent the results from the billiard model for square and rounded junctions with $p = 1$ (solid lines) along with a square junction with $p = 0.7$ and $l'/w = 3$ (dashed line). (b)–(d) Comparisons between experimental R_B (black lines) and billiard model simulations of R_B (solid red lines) for three crosses ($N \gg 1$) using parameters listed in Table II. Simulations with $p = 1$ are shown for comparison (dashed red lines). Inset: A schematic of the geometry used in the simulations. $R_0 = (h/2e^2)(\pi/k_F w_{\text{eff}})$.

$B > 0$ this corresponds to $T_R = T_F = 0$). In our case, a small diffuse background resistance is present, ranging from 20 to 30 Ω (discussed further in Sec. IV E). Before the background resistance is recovered, a small "overshoot" of positive resistance is observed in each cross [indicated by the arrows in Fig. 6(a)], owing to rebound trajectories in rounded junctions, which briefly increase the transmission into the opposite lead. This coincides with the rise in R_H to the last plateau.

The case of NBR in zero magnetic field is useful because the solutions to the LB formulas are simplified, allowing information on the transmission probabilities and collimation to be extracted.[34] At $B = 0$, $T_L = T_R \equiv T_S$ and Eq. (1b) reduces to $R_B(0)/R_0 = (1 - T_F/T_S)/[4(T_S + T_F)]$. For symmetric hard-walled junctions with a fixed geometry (i.e., fixed r/w), the classical model[33] predicts a universal scaling of resistance curves when normalized by R_0 and B_0. In other words, the transmission coefficients (and hence collimation) are approximately equal for geometrically equivalent junctions, and $R_B(0)$ scales inversely with the number of channels $N = k_F w_{\text{eff}}/\pi$ (see Table II). For the purpose of analysis, we define a NBR amplitude $\Delta R_B = R'_B(0) - R_B(0)$ as the difference between the interpolated background resistance at $B = 0$ and $R_B(0)$ [$R'_B(0) = 0$ in the billiard model] [see the inset to Fig. 6(b)]. Figure 6(b) shows the variation of ΔR_B with $1/N$ on a log-log plot. ΔR_B scales approximately, but not exactly, with $1/N$ (indicated by the dashed line). Equally, the scaling predicts that the normalized resistance $R_B(0)/R_0$ is independent of w_{eff} and k_F. Accordingly, in Fig. 7(a) we show

$\Delta R_B/R_0$ plotted against w_{eff} for our devices. Remarkably, we find that $\Delta R_B/R_0$ is almost identical for the largest two crosses: The geometries in these crosses must be equivalent, which is consistent with the assertion that these junctions are approximately square (i.e., r/w_{eff} is small). Scaling of these data is also found for $|B| > 0$ when R_B/R_0 is plotted against B/B_0 (not shown). This is not true for the two smaller crosses, as evidenced by a monotonic increase of $\Delta R_B/R_0$ with decreasing w_{eff}, consistent with the presence of a small but approximately constant rounding that becomes increasingly significant as w_{eff} is reduced. These observations provide valuable insight into the geometry of the junctions, which is used in the billiard model calculations presented in Sec. IV E.

E. Simulation results

To explore further the electron dynamics within the cross junctions, calculations of the bend resistance were performed using the classical model described in Sec. III. Classical and quantum-mechanical calculations of ballistic anomalies in microjunctions have been performed previously by various authors[9,14,30,36] and, as discussed in these works, the geometry of the junction determines the magnitude and character of the resistance anomalies. The parameters in the calculations are w, r, l', v_F, and p [a schematic of the cross geometry is repeated in the inset in Fig. 7(a) for clarity]. The v_F is set by the experimentally determined k_F, and $w \equiv w_{\text{eff}}$ in the model (see Sec. III). We start by considering the magnitude of the experimental NBR and its implications on the collimation in the crosses, and then compare our results for $R_B(B)$ with experimental data.

Simulations of $\Delta R_B(0)/R_0$ for a square ($r/w = 0$) and rounded junction ($r/w = 2$) with specular boundary scattering ($p = 1$) are shown by the solid lines in Fig. 7(a). Recall that no collimation occurs in the square junction, when $p = 1$, whereas collimation is induced in the rounded junction via the horn effect. The experimental $\Delta R_B(0)/R_0$ of the two largest crosses (which we expect to be approximately square) exceeds the calculated values for a square junction by a factor of ~4 and even a rounded junction by a factor of ~2. The anomalously large NBR implies additional collimation is present, other than the horn effect. We attribute this to the *diffuse collimation* effect[20] that results from partially diffuse boundary scattering ($p < 1$) in our devices (as shown in Sec. IV C). The origin of diffuse collimation is the increased backscattering of electrons that enter the leads with large angles ϕ with respect to the lead axis. Therefore, electrons injected with a $\frac{1}{2}\cos(\phi)$ distribution arrive at the junction region after traversing a lead of length l' with a distribution more strongly peaked in the forward direction (hence increasing the ratio T_F/T_S). The resulting angular distribution differs from the horn effect result in that it is more sharply peaked in the forward direction.[30] Consequently, the NBR response $R_B(B)$ for $p < 1$ has a distinctively sharper and more triangular shape about $B = 0$ than in the $p = 1$ case. In support of this conjecture, the experimental data in Fig. 6(a) exhibit the characteristic sharp NBR associated with diffuse collimation.

Billiard simulations with $p < 1$ were implemented using the approach of Ref. 26 (see Sec. III for details). To illustrate the enhancement of the NBR from diffuse collimation, Fig. 7(a) shows a calculation of $\Delta R_B(0)/R_0$ for a square junction with $p = 0.7$ and $l'/w = 3$, as indicated by the dashed line. Remarkably, even for a square junction, the NBR amplitude is increased by a factor of ~5 over the $p = 1$ case, using reasonable parameters. Diffuse collimation is sensitive to the ratio l'/w because this directly influences the number of boundary collisions. In our devices we define l' as the length from the junction to the point at which the lead width flares out [e.g., see Fig. 1(a)]. These values are listed in Table II. Therefore, we can simulate the whole $R_B(B)$ curve by using experimentally determined parameters n, w_{eff}, and l' with only r and p as variables. We perform simulations of the three largest crosses where the classical model is applicable ($N \gg 1$). r is estimated in the range $120 > r > 70$ nm (see Sec. IV D). We note that for a given w_{eff} the position and amplitude of the overshoot in R_B [indicated by the arrows in Fig. 6(a)] is quite sensitive to the value of r, and r was adjusted to best match the experimental feature. Using this method (with $p = 1$ and n, w_{eff}, and l' listed in Table II), we found that $r = 100$ nm yielded reasonable agreement with the experimental data for each cross. This is consistent with the fact that the unintentional rounding results from the fabrication process and sidewall depletion that is approximately independent of w. The value of p was then used as the only fitting parameter to adjust $R_B(0)$ to equal the experimental $R_B(0)$. The results of these simulations (solid red lines) are compared to the experimental data (solid black lines) in Figs. 7(b)–7(d). The agreement with the experimental data is excellent considering the few adjustable parameters involved, validating our experimental determination of w_{eff} and n. Corresponding simulations for $p = 1$ are shown for comparison by the dashed red lines in Figs. 7(b)–7(d), illustrating by contrast the rounded profile of the NBR obtained in the $p = 1$ case. The diffuse background resistance observed in the experimental data is likely to result from the finite momentum scattering time (τ) within the crosses, implying that not all of the electrons are fully ballistic as they are treated in the model ($\tau = \infty$ in the current model). Given the agreement with the ballistic model, we speculate that any momentum scattering in the crosses does not perturb the electron trajectories considerably and therefore the extracted p parameters are meaningful. This is supported by recent work showing that at low temperatures the mobility in these InSb QWs is limited by small-angle remote ionized impurity scattering, i.e., not by phonon scattering that may result in additional backscattering.[17,37]

The values of p used for the three crosses lie in the range from 0.69 to 0.8, which is in good agreement with the value $p \approx 0.7$–0.8 estimated from the measurements on long narrow channels described in Sec. IV C. Moreover, the narrow range of p used in the simulations supports the claim that p is a property of the boundary and thus relatively independent of w for devices fabricated under the same conditions. The incorporation of remote ionized impurity scattering into the billiard model is the subject of further work.

The behavior of the ballistic anomalies described here is transferable to any material system with $p < 1$ (particularly for square cross geometries). However, we emphasize that the partially diffuse boundary scattering reported here is inextricably linked to the particular hard-wall confinement we have achieved in our devices, which exposes the 2DEG to

the etched surface. For example, quite different specularity ($p = 1$) from mesa-etched InSb narrow channels has been reported elsewhere using a different etch chemistry (note that the analysis was limited to $B = 0$).[7] In a quantum-mechanical treatment of boundary scattering,[31] the proportion of diffuse scattering is dependent on the details of the boundary roughness (e.g., the amplitude and correlation length) with respect to the Fermi wavelength, which are likely to vary with the etch chemistry and extent of sidewall depletion. Therefore, it is not surprising that different etch chemistries may yield different results. Our work shows that the ballistic transport properties of InSb mesa-etched devices can be well accounted for within the classical model when the sidewall depletion and realistic partially diffuse boundary scattering are properly addressed.

V. CONCLUSIONS

In summary, we have investigated the variation of the low-temperature transport properties in InSb/$In_{1-x}Al_xSb$ mesa-etched mesoscopic devices with hard-wall confinement when the lateral dimensions are reduced below the mean free path. Measurements on long channels and Hall crosses fabricated from the same sample show that the lateral depletion width is ∼70 nm and that boundary scattering from the sidewall is partially diffuse, with a specularity parameter $p \approx 0.7$–0.8. Ballistic crosses show characteristic resistance anomalies in good agreement with the predictions of the classical model, and in all cases exhibit a significantly enhanced NBR owing to partially diffuse boundary scattering from the sidewalls. Our observations are supported by classical simulations of the electron trajectories in ballistic crosses, which quantitatively accounts for both the magnitude and width of the negative bend resistance, using experimentally determined parameters, and a specularity parameter p in the range 0.69–0.8. Our work highlights the relative importance of diffuse collimation over horn collimation. In particular, the enhancement of the NBR observed in small crosses may be of practical interest for applications requiring large responsivity, e.g., high spatial resolution magnetic-field sensors.

ACKNOWLEDGMENTS

This work was supported by the UK EPSRC under Grant No. EP/F065922/1. S.A.S. is also supported by the US NSF under Grant No. ECCS-0725538, and NIH under Grant No. 1U54CA11934201, and has a financial interest in PixelEXX, a startup company whose mission is to market imaging arrays.

*adam-maurick.gilbertson@ic.ac.uk

[1] S. Datta *et al.*, in *Electron Devices Meeting*, IEDM Tech. Dig. (IEEE International, 2005), p. 763.

[2] S. A. Solin, D. R. Hines, A. C. H. Rowe, J. S. Tsai, Y. A. Pashkin, S. J. Chung, N. Goel, and M. B. Santos, Appl. Phys. Lett. **80**, 4012 (2002).

[3] A. M. Gilbertson, W. R. Branford, M. Fearn, L. Buckle, P. D. Buckle, T. Ashley, and L. F. Cohen, Phys. Rev. B **79**, 235333 (2009).

[4] K. A. Cheng, C. H. Yang, and M. J. Yang, Appl. Phys. Lett. **77**, 2861 (2000).

[5] C. H. Yang, M. J. Yang, K. A. Cheng, and J. C. Culbertson, Phys. Rev. B **66**, 115306 (2002).

[6] J. S. Neal, H. G. Roberts, M. R. Connolly, S. Crampin, S. J. Bending, G. Wastlbauer, and J. A. C. Bland, Ultramicroscopy **106**, 614 (2006).

[7] R. L. Kallaher, J. J. Heremans, N. Goel, S. J. Chung, and M. B. Santos, Phys. Rev. B **81**, 035335 (2010).

[8] M. Büttiker, Phys. Rev. B **57**, 1761 (1986).

[9] H. U. Baranger, D. P. DiVincenzo, R. A. Jalabert, and A. D. Stone, Phys. Rev. B **44**, 10637 (1991).

[10] T. J. Thornton, Superlatt. Microstruct. **23**, 601 (1998).

[11] Y. Takagaki, K. Gamo, S. Namba, S. Ishida, S. Takaoka, K. Murase, K. Ishibashi, and Y. Aoyagi, Solid State Commun. **68**, 1051 (1988).

[12] G. Timp, H. U. Baranger, P. deVegvar, J. E. Cunningham, R. E. Howard, R. Behringer, and P. M. Mankiewich, Phys. Rev. Lett. **60**, 2081 (1988).

[13] M. L. Roukes, A. Scherer, S. J. Allen, H. G. Craighead, R. M. Ruthen, E. D. Beebe, and J. P. Harbison, Phys. Rev. Lett. **59**, 3011 (1987).

[14] C. W. J. Beenakker and H. van Houten, Phys. Rev. Lett. **63**, 1857 (1989).

[15] J. J. Heremans, H. Chen, M. B. Santos, N. Goel, W. V. Roy, and G. Borghs, in *Physics Of Semiconductors: 28th International Conference on the Physics of Semiconductors–ICPS 2006,* edited by W. Jantsch and F. Schaffer, AIP Conf. Proc. No. 893 (AIP, Melville, NY, 2007), p. 1287.

[16] N. Goel, S. J. Chung, M. B. Santos, K. Suzuki, S. Miyashita, and Y. Hirayama, Physica E **20**, 251 (2004).

[17] O. J. Pooley, A. M. Gilbertson, P. D. Buckle, R. S. Hall, L. Buckle, M. T. Emeny, M. Fearn, L. F. Cohen, and T. Ashley, New J. Phys. **12**, 053022 (2010).

[18] C. J. B. Ford, S. Washburn, M. Büttiker, C. M. Knoedler, and J. M. Hong, Phys. Rev. Lett. **62**, 2724 (1989).

[19] T. J. Thornton, M. L. Roukes, A. Scherer, and B. P. Van de Gaag, Phys. Rev. Lett. **63**, 2128 (1989).

[20] R. J. Blaikie, K. Nakazato, J. R. A. Cleaver, and H. Ahmed, Phys. Rev. B **46**, 9796 (1992).

[21] A. M. Gilbertson, Ph. D. Thesis, Imperial College, 2010.

[22] S. E. Laux, D. J. Frank, and F. Stern, Surf. Sci. **196**, 101 (1988).

[23] A. M. Gilbertson, W. R. Branford, M. Fearn, L. Buckle, P. D. Buckle, T. Ashley, and L. F. Cohen, Phys. Rev. B **79**, 235333 (2009).

[24] M. L. Roukes, T. J. Thornton, A. Scherer, and B. P. Vandergaag, in *Electronic Properties of Multilayers and Low-Dimensional Semiconductor Structures*, edited by J. Chamberlain and L. Eaves (Plenum, New York, 1990), Vol. 231, p. 95.

[25] H. van Houten, B. J. van Wees, M. G. J. Heijman, and J. P. Andre, Appl. Phys. Lett. **49**, 1781 (1986).

[26] K. F. Berggren, G. Roos, and H. van Houten, Phys. Rev. B **37**, 10118 (1988).

[27] H. van Houten, C. W. J. Beenakker, P. H. M. van Loosdrecht, T. J. Thornton, H. Ahmed, M. Pepper, C. T. Foxon, and J. J. Harris, Phys. Rev. B **37**, 8534 (1988).

[28] A. B. Pippard, *Magnetoresistance in Metals* (Cambridge Univ. Press, UK, 1989).
[29] E. Ditlefsen, Philos. Mag. A **14**, 759 (1966).
[30] R. J. Blaikie, D. R. S. Cumming, J. R. A. Cleaver, H. Ahmed, and K. Nakazato, J. Appl. Phys. **78**, 330 (1995).
[31] H. Akera and T. Ando, Phys. Rev. B **43**, 11676 (1991).
[32] H. U. Baranger and A. D. Stone, Phys. Rev. Lett. **63**, 414 (1989).
[33] C. W. J. Beenakker and H. van Houten, Phys. Rev. B **39**, 10445 (1989).
[34] L. W. Molenkamp, A. A. M. Staring, C. W. J. Beenakker, R. Eppenga, C. E. Timmering, J. G. Williamson, C. J. P. M. Harmans, and C. T. Foxon, Phys. Rev. B **41**, 1274 (1990).
[35] M. L. Roukes, A. Scherer, and B. P. Van der Gaag, Phys. Rev. Lett. **64**, 1154 (1990).
[36] T. Geisel, R. Ketzmerick, and O. Schedletzky, Phys. Rev. Lett. **69**, 1680 (1992).
[37] J. M. S. Orr, A. M. Gilbertson, M. Fearn, O. W. Croad, C. J. Storey, L. Buckle, M. T. Emeny, P. D. Buckle, and T. Ashley, Phys. Rev. B **77**, 165334 (2008).